A set of high purity chemicals and a number of sophisticated instruments of various characterization techniques were employed, respectively for sample preparations and structure and property investigations.

The preparation of amorphous samples for the present work focuses on two most commonly used techniques viz; (i) Melt quench process and (ii) Sol-gel process. These techniques widely differ from each other. Former is a conventional method for glass preparation whereas the latter is though known for a long time, only recently being used actively for the preparation of inorganic-organic hybrid materials of interest for various applications [1].

2.1 Melt Quench Process

Melt Quench (MQ) process of glass formation utilizes high-temperature treatment by oxy-petroleum flame or similar heat sources to form the glass forming melts (from thoroughly starting materials). The material holder has to be made of a higher melting substance compared to the melting point of the amorphous material being formed. For example, quartz crucibles can be used for the preparation of samples containing starting materials such as PbO, $PbCl_2$, CdO etc. Treatment of starting materials at high temperature leads to the formation of a homogeneous melt in the crucible, and this melt is then immediately poured between thick metallic discs (for example, aluminium discs of approximate thickness of one and a half inch-for the above mentioned case) to form glass samples/flakes. In our case this procedure produces transparent to pale yellow samples of lead glasses, whereas the addition of $CuCl_2$ induces green colour.
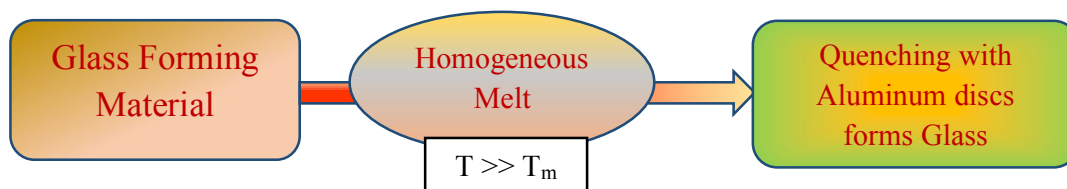

Fig. 2.1 Schematic diagram for sample preparation by Melt Quench method.

By this simple procedure glasses of highly homogeneous nature can be prepared in short time. However, it should be noted that (i) the process requires high temperature to get the homogenous melt and (ii) the quenching rate (the rate at which the melt is lowered in

temperature) can be different from composition to composition. The rate of quenching is very crucial and the important factor in preparation of glass as it determines the nature and quality of the glass.

2.2 Sol-Gel Process

Preparation of glasses by the sol-gel process has several advantages over traditional method of glass formation. The advantages include compositional flexibility, low temperature of processing, homogeneity of materials, high purity. The preparation procedure uses metal-alkoxides ($Si(OR)_4$, R = CH_3, C_2H_5) of metals such as tetraethoxysilane (TEOS: $Si(OC_2H_5)_4$) and tetramethoxysilane (TMOS: $Si(OCH_3)_4$) (for SiO_2) as precursors for the formation of amorphous (glassy) network. Liquid reactants are mixed on a molecular scale and the solution obtained is subsequently solidified into porous amorphous oxide gel. By controlling the conditions of the reaction procedure variable products of interest such as fibres, films, dense ceramics, glasses etc. can be formed. The sol can be cast in form of a film (e.g. by dip coating or spin coating), into a suitable container of any desired shape (e.g. monolithic ceramics, glasses, fibres, membranes, aerogels etc.) or can be used to synthesize powders (e.g. micro-spheres, nano-spheres) [2]. Inorganic or organic hybrid materials can be easily formed by this procedure for various purposes [3-5].

Ebleman [6] in 1846 was the first person to prepare a metal alkoxide starting from $SiCl_4$ and alcohols and identified the gel formation when the alkoxide was exposed to atmosphere. Almost a century later it was shown oxide films can be formed from alkoxides. Network structure of silica gels was accepted in the 1930s; aerogel production by supercritical drying was invented around the same time. Slowly mineralogists, ceramic and nuclear fuel industry scientists started using this process but the developments in nuclear field were published only in 1970s. There were some demonstrations of monolith formations using this process. The technology of the sol-gel process developed in a fast pace but the science of the fundamental aspects of this process is given importance only recently. Further details of this history are available in the book of Brinker and Scherer [7] and the references cited therein.

Starting with the precursors and through sol-gel process one can achieve the metal oxide network-based glasses for many elements and it is observed that ease of gel formation is not connected to ease of glass formation. For example, from zirconium precursors it is easy to form the gel but difficult to get it converted to bulk glass. In the preparations of amorphous zirconium oxide by sol-gel method the densification process is done by layer by layer deposition of thin films followed by annealing or by ion bombardments [8]. Whereas amorphous aluminium oxide is prepared with much less difficulty and with more control in surface area and pore volumes by acetic acid catalysed sol-gel process [9]. SiO_2 based glasses are the most investigated systems due to the excellent capability of both glass formation of SiO_2 and the gel formation of SiO_2 precursors.

Table 2.1 Comparison of glass forming ability of metal oxides by sol-gel process. [10]

Element	Glass Formation	Gel Formation
Silicon	Excellent	Excellent
Titanium	Poor	Excellent
Boron	Good	Poor
Zirconium	Poor	Excellent
Aluminium	Reasonable	Good
Germanium	Good	Good

In the present work, TEOS has been used for the preparation of basic glass network. The steps involved in sol-gel processing are well explained in the review by Hench and West [11]. The seven steps are (i) Mixing (ii) Casting (iii) Gelation (iv) Aging (v) Drying (vi) Dehydration or Chemical Stabilization and (vii) Densification. Of these, the second step, "casting", is required only if we must get the product in a specific shape and hence not considered in this work. In this work, in practice the third and the fourth steps are combined as "aging" is maintaining the gel in its pore liquid (the solvent used in preparing the sol) and it is an extension of the gelation step. Similarly, the step five and six correspond to removal of liquids inside the pores and the silanol hydroxyl group on the surface respectively by different heat treatments. In our work a temperature of 150 ºC is used for the heat treatment and hence the fifth and sixth steps are not complete as will be explained later. 150 ºC is chosen as the drying temperature to avoid the elimination of IL which was confined in the composites during preparation. The last step, "densification", involves high-temperature heating of the gel to form dense glass. In this

process sintering across the pores happens and thus the pores are eliminated, leading to product density equivalent to that of fused silica. The densification temperature can be anywhere between 1000-1700 °C depending on the method of preparation. This step is also avoided in our work for the same reason mentioned above. Thus the formation of silica network in our case practically involves three major steps – (i) to form a homogeneous solution of starting materials (called as sol; sometimes of colloidal suspension nature) in which hydrolysis and polymerization happens (Mixing and Casting), (ii) network condensation in the liquid phase to form a solid gel (Gelation and Aging) and (iii) heat treatment of the gel at 150 °C to partially remove the inner pore solvents and the surface silanol hydroxyl groups (Drying and Dehydration). Even though the steps have been written in a sequential way to understand the glass formation, the chemical and physical events corresponding to some of the steps may happen simultaneously. For example, while condensation is going on hydrolysis may still happen.

2.2.1 Hydrolysis and Polymerization

Silica polymerization can be initiated either in acidic conditions (dil. HCl) or in basic conditions (aqueous NH_3). Acidic and basic solutions are used for catalytic purposes. Kinetics of the reaction is controlled by varying pH of the preliminary solution. Hydrolysis of TEOS occurs around pH ~2-3; at higher pH (~7 or above) weakly acidic anionic monomeric species $SiO(OH)_3^-$ are formed. Further, the rise in pH (~12) gives rise to $SiO_2(OH)_2^{2-}$ species. Based on these observations, Iler [12] defined three different pH domains for the polymerization process i.e. pH < 2, pH 2-7, pH > 7. Isoelectric point/point of zero charges appears at pH 2 (boundary region), where the surface charge on the silica particle becomes zero thereby restricting the electrical mobility of silica particles. At pH 7, solubilities and dissolution rates of silica are maximum. But, on a further rise in pH > 7, particles are ionized which prevents further aggregation or gelation of polymeric units.

Hydrolysis involves the conversion of -OR (where R = C_nH_{2n+1}) group attached to Si to -OH (hydroxyl) group. According to Aelion et. al., acid catalyzed TEOS hydrolysis is first order in H_2O whereas it has zero-order dependence for base catalyzed hydrolysis [13]. Pouxviel and co-workers investigated the acid catalyzed hydrolysis of TEOS for different

molar ratios of H_2O/TEOS (r); the study was done for r = 0.3 (low water), r = 4 (medium water) and r = 10 (high water) systems using ^{29}Si NMR [14]. The observation is with an increase in r, the rate of hydrolysis reaction increases resulting in complete hydrolysis of monomers well before the initiation of condensation process. The sol-gel processing of materials can be done through both hydrolytic as well as non-hydrolytic process [15-16]. The glass composites for present study have been prepared by the processes discussed below.

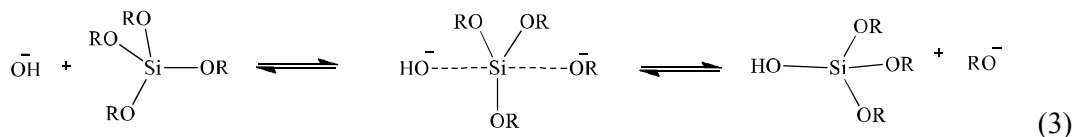**2.2.1a Reaction Mechanism of Hydrolytic Sol-gel Process**

Hydrolysis reactions

(1)
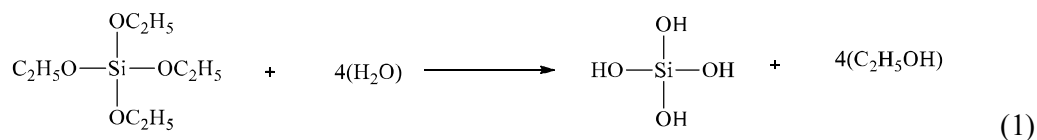
(a) Acid-catalyzed hydrolysis

(2)
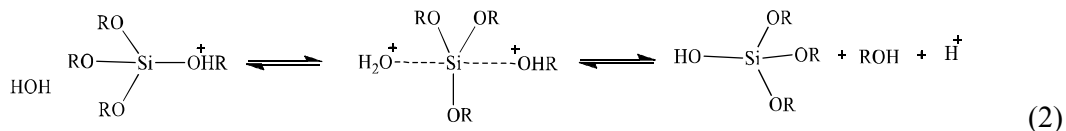
(b) Base-catalyzed hydrolysis

(3)

Procedure followed for sample preparation by hydrolytic process
Acid catalyzed hydrolysis of TEOS is done in acidic medium (HCl at 0.01 equivalent of TEOS) using ethanol as a co-solvent (TEOS: H_2O: EtOH – 1: 4: 10) followed by condensation. After formation of homogeneous sol, $LiNO_3$, $CuCl_2$ and IL were added subsequently. Homogeneous sol obtained from the reaction mixture was kept at ambient conditions to obtain solidified gel (after stiffening of the network). Obtained gel was heat treated initially at 50 °C and then at 150 °C for 15-20 days to form the final composite

(Fig. 2.2). We have avoided the densification step which requires higher temperatures (> 500 ºC) and may eliminate the IL present in the system. Details of chemicals used are given in Table 2.2.
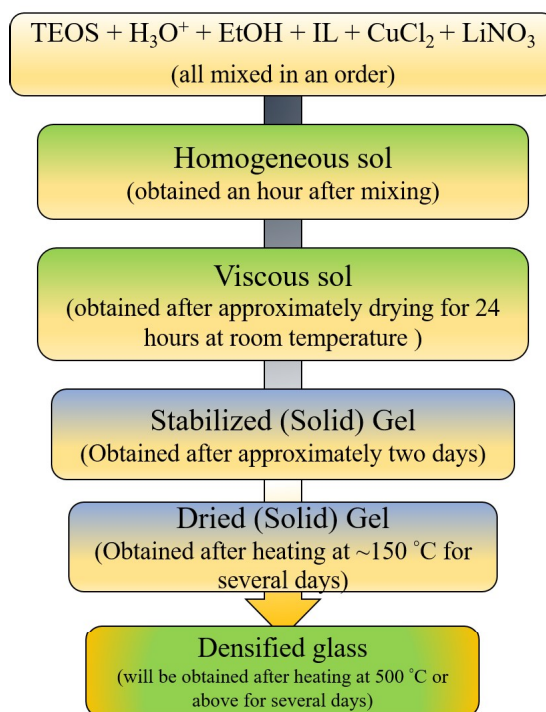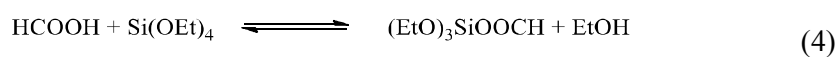

Fig. 2.2 Schematic diagram for hydrolytic sol-gel process

2.2.1b Reaction mechanism of non-hydrolytic sol-gel route

The non-hydrolytic route for sample preparation uses carboxylic acids such as formic acid, which acts as a catalyst, solvent as well as a drying control additive. In general, formation of samples by this process is slow compared to hydrolytic process [5] and hence a better control of the physical and chemical properties of the product is possible. However, for the samples prepared in the current study by this process the gel formation is fast (~30 minutes). Steps involved in this process are as mentioned below.
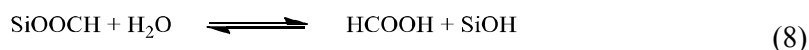
(a) Carboxylation

$$HCOOH + Si(OEt)_4 \rightleftharpoons (EtO)_3SiOOCH + EtOH \tag{4}$$

$$HCOOH + SiOH \rightleftharpoons SiOOCH + H_2O \tag{5}$$

(b) Esterification

$$EtOH + HCOOH \rightleftharpoons EtOOCH + H_2O \tag{6}$$

(c) Hydrolysis

$$SiOEt + H_2O \overset{H^+}{\rightleftharpoons} SiOH + EtOH \tag{7}$$

$$SiOOCH + H_2O \rightleftharpoons HCOOH + SiOH \tag{8}$$

(d) Condensation

$$2SiOH \longrightarrow SiOSi + H_2O \tag{9}$$

$$SiOH + SiOEt \longrightarrow SiOSi + EtOH \tag{10}$$

$$SiOH + SiOOCH \longrightarrow SiOSi + HCOOH \tag{11}$$

$$SiOOCH + SiOEt \longrightarrow SiOSi + EtOOCH \tag{12}$$
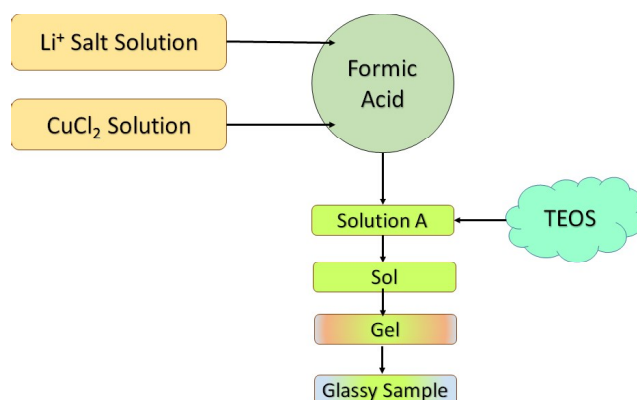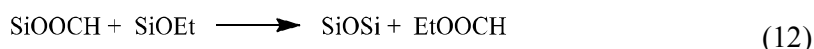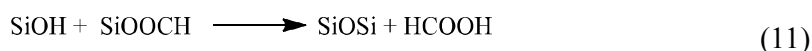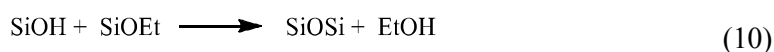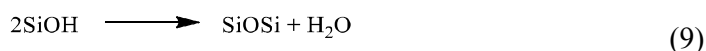

Fig. 2.3 Schematic diagram for Non-hydrolytic sol gel process
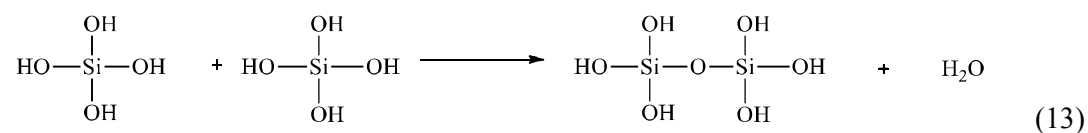
Procedure followed for sample preparation by non-hydrolytic process

Compounds viz; TEOS (Tetraethylorthosilicate), LiNO$_3$ (Lithium nitrate), CuCl$_2$ (Cupric chloride), IL ([EMIM] BF$_4$) have been used as precursors. Hydrolysis followed by condensation of TEOS was done in formic acid, which acted as a catalyst and as a co-solvent. These precursors have been taken in molar ratio of TEOS: HCOOH (1: 8.8). LiNO$_3$, CuCl$_2$ and IL were added subsequently into the reaction mixture while stirring to ensure proper homogeneity of the sol. Homogeneous sol obtained from the reaction mixture was kept at ambient conditions to obtain solidified gel (after stiffening of the network). Obtained gel was heat treated at 150°C for several days to form the final

composite. Again, as mentioned above in the procedure for hydrolytic process of preparation of the composites, we have avoided the densification step (at > 500 ºC) in the non-hydrolytic process also in order to preserve the IL present in the system. Details of chemicals used are given in Table 2.2.

2.2.2 Condensation

Condensation reaction

$$HO-\underset{\underset{OH}{|}}{\overset{\overset{OH}{|}}{Si}}-OH \quad + \quad HO-\underset{\underset{OH}{|}}{\overset{\overset{OH}{|}}{Si}}-OH \quad \longrightarrow \quad HO-\underset{\underset{OH}{|}}{\overset{\overset{OH}{|}}{Si}}-O-\underset{\underset{OH}{|}}{\overset{\overset{OH}{|}}{Si}}-OH \quad + \quad H_2O \tag{13}$$

This follows the hydrolysis process. The network of silica polymer starts condensing with the formation of the 3D network. The process of polymerization to form siloxane bonds and depolymerization (ring opening) goes together. Depolymerisation of the condensing network especially ring structures is required for the formation of a stable gel network i.e. to increase bonding in polymer units. The process of depolymerization is low in water or alcohol medium and prevents breaking of bonds thereby forming stiff 3D-network. Conversion of sol into gel can be determined by the increase in viscosity of the sol. Gelation time is inversely proportional to the average condensation rate. This mainly depends on the pH of the solution [12]. Drying control chemical additives (DCCA) such as formamide are often added in the sol-gel process of glass preparation to alter the rates of hydrolysis and condensation [7]. For example, small amounts of formamide added to methanol solvent, reduces the hydrolysis rate and increases the condensation rate. However, if 50% of methanol is replaced by formamide the situation reverses, i.e., the hydrolysis rate increases, and the condensation rate decreases. We have not used any DCCAs in our work.

2.2.3 Drying and Dehydration

The process of the removal of pore liquids from the gel is known as "drying". During drying the pore liquid is eliminated in three stages: [11] (i) "The constant rate period", where the rate of evaporation per unit area is independent of time; here the volume of the gel reduces by a volume equal to that of liquid lost. Capillary stresses may develop and

to avoid cracks several techniques such as use of surfactants, hypercritical evaporation etc. are employed. (ii) In stage two the network reaches a point where further shrinkage is not possible and hence the liquid transport occurs by flow through the surface films. (iii) In stage three substantial pore liquid is removed and further removal of the liquid requires evaporation inside the pores and diffusion to the surface. The drying process happens below 175 $^{\circ}$C.

Above 175 $^{\circ}$C the process of dehydration takes place (we can also achieve dehydration by chemical treatment with substances such as CCl_4 and consequent heating). In the silica gels the water is present in two forms: (i) free water (alcohol) within the ultraporus gel structure, the physisorbed water, and (ii) bound water on the surface, the hydroxyl (alkoxyl) groups associated with gel surface, the chemisorbed water. The quantity of physisorbed water is directly related to the number of the hydroxyl groups existing on the surface. The dehydration process is completely reversible upto 400 $^{\circ}$C. In our case the solid gel that was formed in the above-mentioned way was initially dried at ambient temperature then at 50 $^{\circ}$C and finally at a higher temperature (150 $^{\circ}$C) for several days. The physisorbed water/ethanol in the ultra-porous gel structure and the chemisorbed water/ethanol at the surface of the composite will not be completely eliminated by the process of heat treatment at 150 $^{\circ}$C; heat treatment beyond 400 $^{\circ}$C is required to irreversibly eliminate the entire hydroxyl group containing components and only beyond 800 $^{\circ}$C, complete elimination of hydroxyl and ethoxy ($-OC_2H_5$) groups are expected. As mentioned earlier 150 $^{\circ}$C is chosen as the drying temperature to avoid the elimination of IL from the composite. We find from IR spectroscopy and from other evidence the presence of water both in the surface and the inner pores. The amount of water in the inner pores is more than the surface water. Also, to avoid the irreversible loss of water/hydroxyl groups and the IL during various experiments such as electrical conductivity measurements, the temperature was maintained below 350 $^{\circ}$C during such measurements.

In the present work, the effect of confining the following three ILs in the silica gel systems have been explored.

1. 1-butyl-3-methylimidazolium bromide [BMIM] Br
2. 1-ethyl-3-methylimidazolium tetrafluoroborate [EMIM] BF_4

3. 1-ethyl-3-methylimidazolium trifluoromethanesulphonate [EMIM] CF_3SO_4

Table 2.2. Chemicals used in this work.

S. No.	Compound Name	Molar Mass (g mol^{-1})	Melting Point (°C)	Boiling Point (°C)	Density (g cm^{-3})
1.	Lead Oxide (PbO)[a, #]	223.2	888	1,477	9.53
2.	Lead Chloride (PbCl$_2$)[a, #]	278.10	501	950	5.85
3.	Cadmium (II) Chloride (CdCl$_2$)[a, #]	183.31	568	964	4.047
4.	Cadmium Oxide (CdO)[a, #]	128.41	128.41	1,559	8.15
5.	Cupric Chloride (CuCl$_2$.2H$_2$O)[a, $]	170.48	498	993	3.39
6.	Carbon tetrachloride (CCl$_4$)[a, #]	153.81	22.92	76.72	1.586
7.	Lithium Carbonate (LiCO$_3$)[a, *]	73.89	723	1,310	2.11
8.	Tetraethylorthosilicate (TEOS)[c, #]	208.33	85	168	0.934
9.	Lithium Chloride (LiCl)[a, #]	42.39	610	1,382	2.068
10.	Lithium Nitrate (LiNO$_3$)[b, #]	68.94	255	600	2.38
11.	Lead Nitrate (Pb(NO$_3$)$_2$)[b, #]	331.2	470	-	4.53
12.	1-butyl-3-methylimidazolium bromide [(BMIM) Br][c, #]	219.12	65-75	>250	1.287
13.	1-ethyl-3-methylimidazolium tetrafluoroborate [(EMIM) BF$_4$][c, #]	197.97	15	>350	1.294
14.	1-ethyl-3-methylimidazolium trifluoromethanesulphonate [(EMIM) CF$_3$SO$_3$][c, #]	260.23	-10	>350	1.387

a – MOLYCHEM, INDIA, b – MERCK, c – *Alfa Aesar*
- Used as it is in the composites, $ - Used in proportion to obtain $CuCl_2$, * - Used in proportion to Li_2O.

2.3 Characterization and analytical techniques

Instrumentation used for the detailed analysis and characterization of the prepared amorphous systems are briefly mentioned below.

2.3.1 X-Ray Diffraction

X-Ray diffraction is one of the important techniques that gives the details of the atomic level structure of materials [17-18]. X-rays are electromagnetic waves with a wavelength that matches to the atomic distances in the crystal planes ($\lambda \leq 2d$, where λ is wavelength

and d is the distance between planes). The wavelength comparable to that of the distance between atom positions in the lattice planes makes it possible to diffract the X-ray when it interacts with the crystals. On exposure of any atom to X-rays, two different types of scattering occur. The tightly bound electrons scatter X-rays of the same wavelength as of incident rays, they are expressed in terms of atomic scattering factor (*f*), (coherent / unmodified scattering), whereas the loosely bound electrons scatter X-rays with slight increase in wavelength depending upon scattering angle (incoherent / Compton modified scattering). Coherent scattering from samples produces diffracted beams that can be expressed in the form of XRD pattern.

The well-known Bragg's law of diffraction is

$$n\lambda = 2d\sin\theta \qquad [1]$$

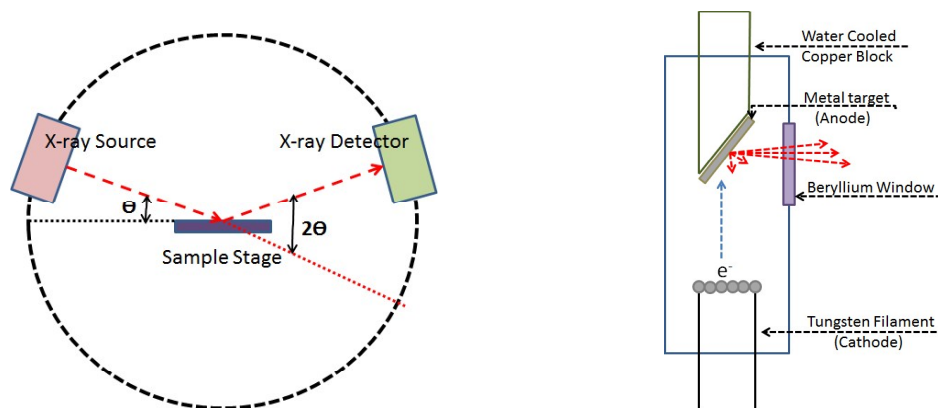and here θ is the angle of diffraction.

Fig. 2.4 X-ray diffractometer (block diagram) and x-ray tube

PXRD (Powder X-ray Diffraction) pattern is obtained when the sample is in powder (polycrystalline) or amorphous forms. In this work we do not deal with single crystal X-ray diffraction and the focus is on PXRD only.

Broadly, PXRD patterns of polycrystalline materials (powders of single crystals) provide the following important information:

1. The set of position of peaks in a pattern relates to set of planes of crystal lattice.

2. Broadening/missing of the peak accounts for some defect/strain in the lattice.

3. The intensity of the samples is proportional to the planar density of the atoms.

4. Full-width at half-maximum (*FWHM*) of a peak corresponds to the particle size of the crystals. (This point is elaborated further below.)

The width of the peak increases with a decrease in the thickness of crystal (t). Peak width (B) can be measured in terms of radians at an intensity equal to FWHM; this can be also measured from the extreme ends of the peak at angles $2\theta_1$ and $2\theta_2$ where the peak intensity is close to zero.

$$B = \frac{1}{2}(2\theta_1 - 2\theta_2) = \theta_1 - \theta_2 \qquad [2]$$

Path difference at these two angles is

$$2t \sin \theta_1 = (m + 1)\lambda \qquad [3]$$

$$2t \sin \theta_2 = (m - 1)\lambda \qquad [4]$$

Subtraction of eq. [4] from [3]

$$t (\sin \theta_1 - \sin \theta_2) = \lambda \qquad [5]$$

$$2t \cos \left(\frac{\theta_1 + \theta_2}{2}\right) \sin \left(\frac{\theta_1 - \theta_2}{2}\right) = \lambda \qquad [6]$$

but, θ_1 and θ_2 are nearly equal to θ_B. So,

$$\theta_1 + \theta_2 = 2\theta_B \qquad (approx.) \qquad [7]$$

and

$$\sin \left(\frac{\theta_1 - \theta_2}{2}\right) = \left(\frac{\theta_1 - \theta_2}{2}\right)(approx.) \qquad [8]$$

Therefore,

$$2t \left(\frac{\theta_1 - \theta_2}{2}\right) \cos \theta_B = \lambda \qquad [9]$$

$$t = \frac{\lambda}{B \cos \theta_B} \qquad [10]$$

An exact treatment will give the value as, $t = \frac{K\lambda}{B \cos\theta_B}$ where K is a dimensionless shape factor having value close to unity (0.9 is normally used) [11]. This is known as Scherer formula, which can be used to determine the size of the particle from the measured width of the diffraction curve.

RIGAKU MiniFlex II with CuK_α radiation (λ = 1.54 Å) at room temperature was used for structural analysis of the samples. PXRD measurements were performed at a voltage of 30 kV with a filament current of 30 mA. The instrument is tailored with K_β filter foil (does not have Ni filter) along with graphite monochromator. Diffraction patterns were recorded at a speed of (1-3) º /min (2θ) depending on the requirement.

2.3.2 Electron Paramagnetic Resonance (EPR) Spectroscopy

Transition frequency between different spin states of an unpaired electron can be measured by EPR spectroscopy (also known as ESR –Electron Spin Resonance Spectroscopy) [19-20]. In the strong magnetic field, the degeneracy of electronic spin states $m_s = \pm 1/2$ is removed, known as Zeeman splitting. Excitation energy of the transition depends on the extent of splitting i.e. on the applied magnetic field. Energy levels of a free electron are different from that of the paired electrons. Hence, the corresponding g-factor (Landé g factor) differs from that of the free electron (g_e = 2.0023) and is defined in terms of orbital angular momentum (L) and total angular momentum (J):

$$g = 1 + \frac{S(S+1) - L(L+1) + J(J+1)}{2J(J+1)}$$

The coupling can happen between electron and nuclear spins, known as "hyperfine coupling". The g-factors, hyperfine coupling constants, the line shape etc. of the EPR spectra, reveal a lot of information regarding the electronic and structural environment of the source of absorption. In the present work Cu^{+2} has been doped into the glassy/gel matrices as an EPR probe to get the structural information of these composites. Measurements were done on ESR spectrometer JEOL, Japan (JES-FA200 ESR Spectrometer in X (9 GHz) and Q (32 GHz) band microwave region)

Paramagnetic species in an applied magnetic field resonate on interaction with the electromagnetic radiations and the resonance condition relation can be expressed as

$$hv = g\beta H_0 \qquad\qquad (1)$$

where β is the Bohr magneton and H_0 is the applied magnetic field. In amorphous systems the inhomogeneous broadening of the spectral line is due to the distribution of the EPR species in large number of structural sites with very small variation in environment and bonding between sites. By multi-frequency EPR studies the statistical parameters of this distribution can be estimated [19, 21-22].

Fig. 2.5 ESR spectrometer JEOL, Japan (JES-FA200).

The magnetic resonance spectrum of a solid sample is recorded as the first derivative of resonant absorption versus the applied magnetic field, **H**. From this special 'shape' one then derives the appropriate 'spin Hamiltonian', which is nothing but an expression in matrix representation for the interaction energy of the paramagnetic spin vector (nuclear spin **I** in the case of NMR and electron spin **S** in the case of EPR) with the field vector, **H.** The various parameters of the spin Hamiltonian are then related back to the chemical bonding of the environment by means of appropriate theories of molecular electronic structure.

The aforementioned spin Hamiltonian denoted in its most general form by $\hat{H}_{EPR}$, is phenomenological set up such that it has a leading term representing the 'Zeeman' interaction between **H** and the **S** or **I** spin vector, followed by successively smaller 'perturbations' representing various tensorial couplings. In EPR, it takes the most general form

$$\hat{H}_{EPR} = \beta_e \boldsymbol{H} \cdot \boldsymbol{g} \cdot \boldsymbol{S} + \boldsymbol{I} \cdot \boldsymbol{A} \cdot \boldsymbol{S} + \boldsymbol{S} \cdot \boldsymbol{D} \cdot \boldsymbol{S} + \boldsymbol{I} \cdot \boldsymbol{Q} \cdot \boldsymbol{I} - \gamma \hbar \boldsymbol{I} \cdot \boldsymbol{H} \qquad (2)$$

Where the leading (or zero order) Zeeman term defined the molecular g – tensor. The second term is the electron spin-nuclear spin 'hyperfine' interaction (**A**), and the third term (operative in the case of several unpaired electron spins being present in the valence orbital of the paramagnetic center, e.g., Mn^{+2}) is the 'fine structure' (or crystal field) interaction (**D**). the last two terms of (2) are the nuclear quadrupolar (**Q**) and the nuclear Zeeman interaction, respectively, and are usually very small members in the above 'hierarchy' of perturbation   and could become important in special instances. In (2) β_e is the fundamental 'electronic Bohr magneton' unit, and γ is another fundamental interaction constant called the nuclear magnetogyric ratio. g, **A**, **D** and **Q** are symmetric second-rank tensors representing the anisotropic nature of the respective couplings. In this work as mentioned earlier Cu^{2+} (d^9 system with one unpaired electron) is used as the probe and hence only the first two terms of the spin Hamiltonian are considered. The EPR resonance condition (m_s -1 $\rightarrow$ m_s with $\Delta m_I = 0$) to first order is

$$hv = g\beta_e H + (Am/g) \tag{3}$$

where,

$$g = [g_1^2 sin^2\theta sin^2\varphi + g_2^2 sin^2\theta cos^2\varphi + g_3^2 cos^2\theta]^{1/2} \tag{4}$$

$$A = [A_1^2 g_1^2 sin^2\theta sin^2\varphi + A_2^2 g_2^2 sin^2\theta cos^2\varphi + A_3^2 g_3^2 cos^2\theta]^{1/2} \tag{5}$$

Given below is a brief description of a procedure developed by Peterson and co-workers [24], to simulate the EPR spectra of glasses. The collection of all the paramagnetic species, each with an individual geometry ω_i, is denoted by Ω. For a simple 'g-only' case with axial symmetry, each of these ω_i can be mapped on to Euclidean three-shape by a random vector **X** whose components are $g_\parallel$, $g_\perp$ and θ. θ is the angle between the magnetic field direction and the principle symmetry axis. The components of **X** can be described by a joint probability density function, p ($g_\parallel$, $g_\perp$, θ). Since θ is statistically independent of $g_\parallel$ and $g_\perp$, we have

$$\boldsymbol{p\,(g_\parallel, g_\perp, \theta) = p(g_\parallel, g_\perp) \cdot p(\theta)} \tag{6}$$

$\boldsymbol{p(\theta)}$ is a well-known function *sin θ* in the domain θ = 0 to $\pi/2$, $\boldsymbol{p(g_\parallel, g_\perp)}$ is assumed to be bivariate normal density function with $\sigma_\parallel^2, \sigma_\perp^2$ as the variances and p as the correlation

coefficient between $g_\parallel$, and $g_\perp$. The objective is to find out the probability density function of the magnetic field from the above given densities, such that the following resonance condition is satisfied

$$hv = g\beta_e H = \left[g_\parallel^2 cos^2\theta + g_\perp^2 sin^2\theta\right]^{1/2}\beta_e H \qquad (7)$$

and this is achieved as follows. First the random vector **X** is transformed into a new random vector **Y** whose components are $g_\parallel, g_\perp$ and g. The new vector is described by the density function

$$p\left(g_\parallel, g_\perp, g\right) = p(g_\parallel, g_\perp) \cdot p(\theta)|J| \qquad (8)$$

Where $|J|$ is the absolute value of the Jacobian associated with the transformation.

Now, the probability density of g is given by [21]

$$p(g) = \iint p\left(g_\parallel, g_\perp, g\right)dg_\parallel \, dg_\perp \qquad (9)$$

The domain of this integration has to be carefully fixed because it depends on how **X** has been transformed into **Y**. In the integration, one has to avoid the singularities at $g_\parallel = g_\perp$, and $g_\perp = g$. The final step in the above computation is to convert the density g into that of magnetic field **H** as given by

$$p(H) = p\left(g\right) \cdot \left|\frac{hv}{\beta_e H^2}\right| \qquad (10)$$

Where, once again, $\frac{hv}{\beta_e H^2}$ is the Jacobian associated with the transformation. The last-mentioned transformation is essential for explaining the spectra recorded at different frequencies.

A new formalism developed by Raghunathan and Sivasubramanian [21] all the three above mentioned steps [viz; (i) derivation of the Jacobian and transformation of the random vector into another domain; (ii) integration of the transformed joint density to get the density of g, and (iii) transformation of the g density to H-density] are automatically realized. In this approach, given the overall joint density of the random variables $x_1, x_2, \ldots\ldots, x_n$ and the relation between these and a new variable z such as, say, $z = h(x_1, x_2, \ldots\ldots, x_n)$, the density of z, namely $f(z)$, is given by

$$f(z) = \frac{1}{dz}\iint_{\Delta D_z}\cdots\int f(x_1, x_2,\ldots x_n)dx_1, x_2,\ldots x_n \tag{11}$$

In (11), the domain of the integration, ΔD_z, is defined by the inequality

$$z < h(x_1, x_2,\ldots x_n) \le z + dz \tag{12}$$

Using (11), the density of H can be written as

$$p(H) = \frac{1}{dH}\iiint_{\Delta D_H}p(g_\parallel, g_\perp)\, p(\theta)dg_\parallel\, dg_\perp\, d\theta \tag{13}$$

Where, ΔD_H is our domain of interest described by

$$H < h\nu\Big/\Big[\big(g_\parallel^2\cos^2\theta + g_\perp^2\sin^2\theta\big)^{1/2}\beta_e\Big] \le H + dH \tag{14}$$

Equation (13) is seen to be a triple-integral. The domain will have to be fixed by imposing our 'resonance condition' according to (14) as the upper and lower limits on one of the integrals. We find it easier to solve for θ given $g_\parallel, and\ g_\perp$ and H (or H+dH). Similarly,

$$p(H) = \frac{1}{dH}\int_{g_1}^{g_2}\int_{g_3}^{g_4}p(g_\parallel, g_\perp)\, dg_\parallel\, dg_\perp\int_{\theta_1}^{\theta_2}\sin\theta\, d\theta \tag{15}$$

In (15) the limits for $g_\parallel, and\ g_\perp$ are fixed by truncation of $p(g_\parallel, g_\perp)$ such that beyond the truncated limit $(g_1, g_2\ for\ g_\parallel\ and\ g_3, g_4\ for\ g_\perp)$ the density is negligible. After truncation, we normalize the density and carefully define the density only in the positive quadrant; that is $g_\parallel, and\ g_\perp$ are always given as positive non-zero numbers. The upper and lower limits of θ where the resonance condition is imposed are given as

$$\theta_1 = \sin^{-1}\Big\{\big[(h\nu/\beta_e H)^2 - g_\parallel^2\big]/\big(g_\perp^2 - g_\parallel^2\big)\Big\}^{1/2} \tag{16}$$

and $$\theta_1 = \sin^{-1}\Big\{\big[(h\nu/\beta_e(H+dH))^2 - g_\parallel^2\big]/\big(g_\perp^2 - g_\parallel^2\big)\Big\}^{1/2} \tag{17}$$

Probability density function for describing the distribution of spin Hamiltonian parameters is normally a Gaussian distribution and it can be univariate or multivariate with or without correlation.

The line broadening in EPR spectra has been studied from the time Portis [25] explained the broadening in Crystals having F-centers. Broadening of lineshapes can be either homogeneous or inhomogeneous [25-26]. Homogeneous broadening is caused by (i) dipolar interaction between like spins, (ii) spin-lattice relaxation, (iii) interaction with the radiation field, (iv) motion of carriers in the microwave field, (v) diffusion of excitation through the sample, (vi) motionally narrowed fluctuations in the local field, etc. In homogeneous broadening, the energy absorbed from the electromagnetic radiation field is distributed to all the spins and thermal equilibrium of the spin system is maintained through resonance. Inhomogeneous broadening occurs when inhomogeneity exceeds the natural line width. This occurs due to (i) unresolved fine structure, (ii) Hyperfine structure, (iii) Dipolar interaction between spins with different Larmor frequency, etc. Here the line width arises due to variations in the local magnetic fields and the EM radiation energy will be transferred only to those spins whose local fields satisfy the resonance condition. In the present work Cu^{2+} is the only paramagnetic ion present in the system and also at a lower concentration (1 mol%) and hence dipolar broadening is minimized. In the simulations of the spectra one normally utilizes a Lorentzian shape function for homogeneous broadening and a Gaussian shape function for inhomogeneous broadening. In some cases, other shape functions are also used.

EPR spectra of amorphous materials show broadening of lines in a way which is different from that of crystalline or polycrystalline (powder) samples. This becomes evident when multi frequency studies of the same sample are performed. In general, in magnetic resonance experiments when the frequency of absorption is increased, the broadening decreases due to many reasons; specifically as the Zeeman splitting is increased, the lower level population increases, field independent couplings such as hyperfine couplings get separated, second and higher order effects are minimized, and these lead to increasing the intensity and resolution and reducing the broadening of spectral lines. This happens as expected in the spectra of crystalline or polycrystalline substances. However, in amorphous materials the reverse happens, i.e., the broadening increases with increasing frequency and better resolved spectra are obtained at lower frequency. This is due to the inhomogeneous broadening of the spectral line arising from the distribution of the EPR probe in large number of structural sites with very small variation in environment and bonding from site to site. The "random structure model" based spectral

simulation described above is able to produce the multi frequency spectra of the sample with same statistical parameters. No shape function is used here. For fixed statistical parameters only, the frequency is changed to get different spectra. The statistical parameters thus obtained may reveal about the randomness of the amorphous structure. The simulations were performed by using FORTRAN based software developed in in-house.

2.3.3 Fourier Transform Infrared (FTIR) spectroscopy

Infrared spectroscopy is the study of interaction infrared light with a molecule or a substance. This is well known technique used by organic and inorganic chemists and material scientists to get the vibrational frequencies of a molecule and through that bonding information [27]. Hooke's law is used to determine the fundamental vibrations of diatomic molecules. For the harmonic oscillator, vibration frequency can be expressed as

$$\bar{\nu} = \frac{1}{2\pi c}\sqrt{\frac{K}{\mu}}$$

Where, c = speed of light, K = force constant, and μ = reduced mass (m1.m2/(m1+m2)). Molecules with stronger bonds with light atoms vibrate at a high stretching frequency. Only vibrations where the electric dipole moment changes during the vibration are visible in this technique. To identify other vibrations techniques such as Raman Spectroscopy has to be used.
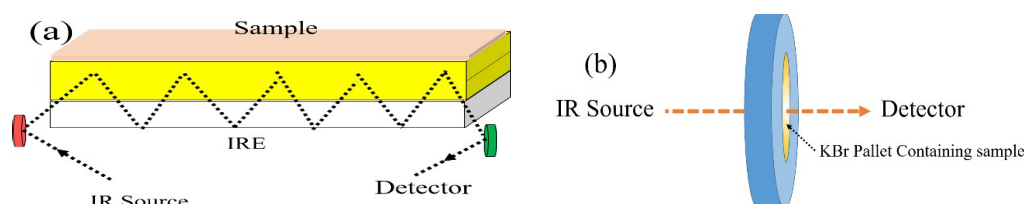
Fig. 2.6 Schematic diagram for sample analysis in FTIR Spectrophotometer in (a) ATR mode and (b) Transmission mode.

IR spectra of samples can be recorded in two modes (i) ATR (Attenuated Total Reflectance) mode where a minute quantity of the sample is directly kept on the diamond sample holder; (ii) the more popular transmission mode in which the IR radiation passes

through pellets made of 5% sample mixed in dry KBr. In the ATR mode IR attenuation (absorption) happens up to 5 μm depth only. Thus, the ATR spectra provide the surface information and the transmission mode spectra correspond to the bulk of the sample (schematic of both in Fig. 2.6). FTIR measurements have been done on IRAffinity-1S instrument from SCHIMADZU in both ATR and transmission mode in the range 400 - 4000 cm^{-1}.

2.3.4 Field Emission Scanning Electron Microscopy (FESEM)

Field Emission Scanning Electron Microscopy is one of the important techniques to study the surface of the solid materials [28]. In this technique, electrons which are liberated by a field emission source and accelerated in a high electrical field gradient are used to scan the surface of the object. Primary electrons are focused and deflected by the electronic lenses to produce a narrow beam of electrons that bombards on the surface of the object. This results into emission of secondary electrons from the surface of the object. The topography of the surface is determined by the variations in angle and velocity of the electrons which are measured by the detector. Secondary electrons are detected under standard detection mode of the equipment which gives details for size even <1nm. In the present work, FESEM analyses were done using Thermo Fisher Scientific FEI Apreo-S instrument.

For analysis sample should be electronically conductive; non-conductive samples are coated by thin conductive layer (Gold, carbon, platinum etc.) before being used for the analysis.

Energy Dispersive X-ray Spectroscopy (EDS/EDX - elemental mapping): This technique has been used to understand the elemental composition and the chemical characterization of the sample surfaces. X-rays are emitted when the scanning electron beam knocks off an inner shell electron, causing a higher-energy electron to fill the shell and release energy. The energies of the X-ray photons are characteristic of the element which produced it. The EDS X-ray detector measures the number of emitted X-rays versus their energy. The above-mentioned equipment has the provision to record the EDX spectra.
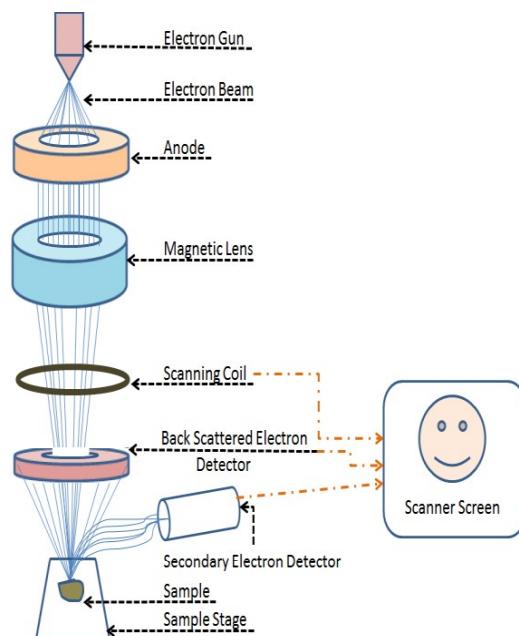
Fig. 2.7 Schematic Diagram of Scanning Electron Microscope.

2.3.5 X-Ray Photoelectron Spectroscopy (XPS)

X-Ray Photoelectron Spectroscopy (XPS) is often used in analyzing the surface composition of the samples and can be applied to a wide range of materials [29-30]. It measures the elemental composition, chemical state, electronic state of the material. In the analytical process, the material is irradiated with a beam of X-rays which knocks out the surface electrons; kinetic energy and number of electrons are measured to produce XPS spectrum (penetration depth: 0-10 nm).
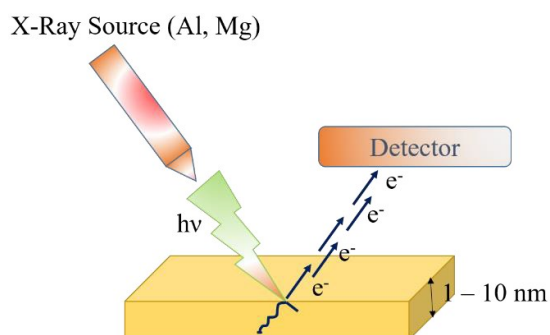
Fig. 2.8 Schematic Diagram of XPS.

In the present work the instrument used for X-ray photoelectron spectroscopy is Omicron ESCA (Electron Spectroscope for Chemical Analysis) from Oxford Instrument Germany. Measurements have been performed using 400 mesh C-coated Cu grid followed by 24 hours degassing. Omicron EA 125 with Al Kα radiation (1486.7 eV) was used as a source for the measurements. Monochromatic nature of X-ray is confirmed with a FWHM about 0.60 eV. At the time of sample analysis, the emission current of the X-ray source and the anode voltage were fixed at 20 mA and 15 kV respectively. High-resolution XPS spectra have been recorded with a step size of 0.02 eV and energy of 20 eV. C 1s binding energy peak at 284.5 eV was set as a reference to balance any kind of charging effect. Angle between the analyzer and the source is maintained at approximately 85 ^{o}.

2.4 Thermal Studies

Thermal behavior of the sample is studied qualitatively and quantitatively by different thermal analyzing techniques as a function of temperature. The techniques used are Differential Scanning Calorimetry (DSC), Differential Thermal Analysis (DTA) and Thermo-Gravimetric Analysis (TGA).

2.4.1 Differential Scanning Calorimetry (DSC)
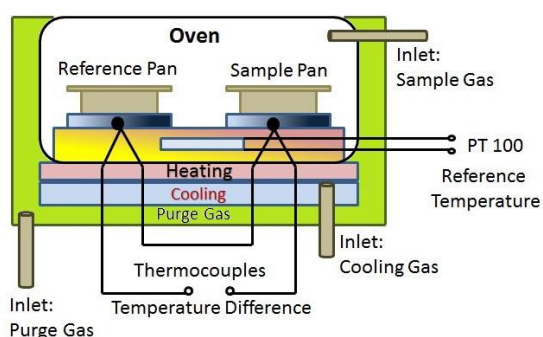
Fig. 2.9a Schematic diagram of DSC instrument   Fig. 2.9b DSC scan for glassy sample
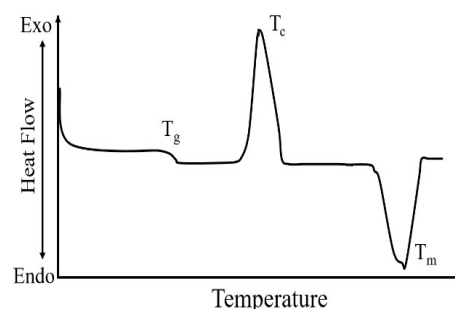
This is a thermo-analytical technique which measures the heat flow rate changes occurring between a sample and an inert reference as a function of temperature [31]. Differential Scanning Calorimeters can be broadly classified in two categories as (i) Heat Flux instruments and (ii) Power Compensation instruments, based on the method by which these instruments measure the change in the heat flow rate.

During analysis, the temperature is increased for both the sample as well as the reference at a constant rate and pressure. Enthalpy changes (heat flow) can be observed as:

$$\left(\frac{dq}{dt}\right)_p = \left(\frac{dH}{dt}\right)$$

where (dH/dt) is Heat flow mcal sec^{-1}. Therefore, heat flow difference between sample and reference can be measured as:

$$\left(\frac{\Delta dH}{dt}\right) = \left(\frac{dH}{dt}\right)_{Sample} - \left(\frac{dH}{dt}\right)_{Reference}$$

Here, (ΔdH/dt) could be positive (endothermic process) for heat absorbed events or negative (exothermic process) for heat evolving events. Both the reference and the sample are kept at a nearly constant temperature by a controlled temperature program, and any variation in the enthalpy release is measured. The behavior of sample with respect to the change in temperature is understood by corresponding exo/endothermic peaks. Enthalpy release corresponds to thermal events such as crystallization temperature (T_c) and enthalpy gain indicates events such as glass transition (T_g), melting temperature (T_m) in the samples. Along with determining thermal events, reaction kinetics, the activation energy of the reaction, specific heat capacity and phase transitions can also be explored. For the present work, measurements were done on DSC 60 plus series SHIMADZU, with heating rates of 5, 10, 20, 30 °C/minute (for chapter 3 samples) and with 10 °C/minute (for chapter 3 samples) to understand their thermal behavior and kinetics. Some low temperature DSC measurements, which were necessary to confirm the confinement of IL in the gels, have been performed with temperature modulated differential scanning calorimeter (TA Instruments, Model 2910).

2.4.2 Differential Thermal Analysis (DTA)

This is an another thermoanalytical techniques similar to DSC, used to understand the thermal properties and events of the samples [32]. For the present studies DTA 60 series (SCHIMADZU) instrument has been used for the analysis under nitrogen atmosphere with the heating rate of 10 °C/minute. In DTA under identical heating conditions the temperature difference between a inert reference and the sample are determined as a

function of time or temperature which in turn will relate to heat absorbed or evolved. Thus, endothermic or exothermic changes in the samples with respect to the inert refernce are detected and the differential temperature is then plotted with respect to time or temperature.
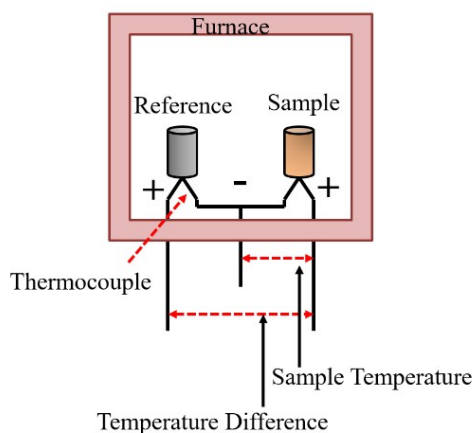

Fig. 2.10 DTA 50 plus series SHIMADZU setup.

For an endothermic change, the temperature of sample is lower than the temperature of refernece (ΔT = -ve) whereas in an exothermic event, the sample temperature is high (ΔT = +ve). The area under the peak corresponds to enthalpy change and is not affected by the heat capacity of the sample.

2.4.3 Thermo-gravimetric Analysis (TGA)

Chemical and physical changes in samples can be readily detailed as a function of the change in increasing temperature with the constant heating rate or as a function of time with constant temperature and mass loss [32]. Results of the analysis determine second-order phase transition properties of the materials. Weight loss or gain from the sample is because of several events like decomposition, oxidation or loss of volatiles. This technique further helps in understanding thermal events in the samples within a desired temperature range and points to the type of physical or chemical process corresponding to the event.

The instrument of TGA consists of a sample pan attached to a heater and a precise micro-balance. Pan is heated and cooled during the experiment to record the thermal events. Thermally stable samples exhibit no weight loss with the rise in temperature.
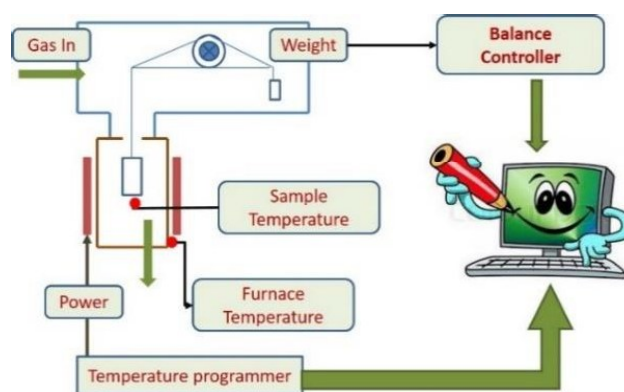

Fig. 2.11 Schematic Diagram of TGA instrument.

Measurements were done on TGA 60 plus series SHIMADZU, with heating rates of 2°C for sol-gel samples and 10 °C for melt quench prepared samples.

2.5 Electrical Characterization

2.5.1 Electrical Conductivity

Electrical conductivity (σ) is the measure of the flow of charges through any material. Based on conducting capacity, materials can be conductors, semiconductors and insulators. This classification is based on the available band gaps through which conduction occurs either by holes or by the electrons. Conductivity is expressed as $\sigma = l/RA$, where l is thickness, R is the resistance and A is the area (cross-sectional) of the sample. Its SI unit is Siemens per meter (S/m).

Dynamic as well as steady state electrical conductivity has been measured with computer interfaced HIOKI LCR meter (3532-50). For dynamic studies the heating rate was controlled using electric Libratherm PID controller model PRC-309.

The sample holder is made from lava stone, Teflon discs, two stainless steel electrodes, stainless steel support rods. A pair of chromel-alumel thermocouple has been used as the temperature sensor. The conductivity measurements have been done in blocking

electrode configuration, where silver paste has been used as an electrode to frame up the conductivity set up.

1. Teflon Disc
2. Pressure Spring
3. Thermocouple (Chromel-alumel)
4. Quartz Tube
5. Stainless steal rods
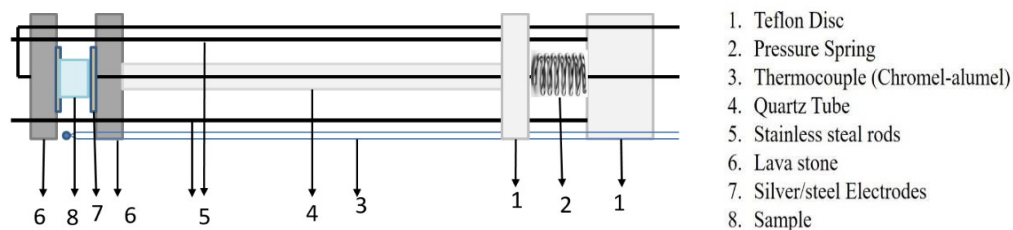6. Lava stone
7. Silver/steel Electrodes
8. Sample

Fig. 2.12 Schematic diagram of sample holder used for electrical conductivity measurements (300K – 1000K).

Measurements were done with a heating rate of 1 ^{o}C/min, in the temperature range of RT - 400 ^{o}C on cylindrical pellets. The dc-voltage motion of ions is very fast which leads to polarization at the electrode-electrolyte interfaces, making sample resistive with time. This non-steady state does not help in determining the bulk resistance of the sample. To overcome this disadvantage, ac-voltage has been used; this technique is known as Impedance Spectroscopy (discussed below).

2.5.2 Impedance Spectroscopy [33]

In electrical engineering, plotting of ε' and ε'' for dielectric systems in the complex plane is known as Cole-Cole plot. It was also used and explained in the field of semiconductors, ionic systems, and devices and was termed as Nyquist plots. Sluyters and Oomen [34-35] for the first time plotted the impedance for liquid electrolytes to understand the process of ion transport in bulk conducting samples. Bulk properties such as, in grain conduction, grain boundary conduction, ion transport, relaxation and another interfacial phenomenon were explored. Impedance measurement is highly efficient for solid electrolytes, and an interface in a solid-state cell polarizes on applying an electric signal.

Electrode and electrolyte are the two different components of the cell. Polycrystalline cell components exhibit interfaces between their grains. AC current signal applied to the cell informs about different interfaces in the cell. This information is given in terms of

Impedance [33]. For DC circuit, R=V/I known as resistance whereas in AC circuit, Z=V/I known as impedance.

Conventionally impedance measurements were done as a function of the frequency of the applied electric field. AC voltage, $V(\epsilon) = V_m \sin(\omega t)$, with a single frequency applied ($\omega=2\pi f$ is the angular frequency). Corresponding steady state current $i(t)=I_m \sin(\omega t+\vartheta)$ was measured. Where ϑ is the phase difference between the voltage and the current and is zero for pure resistors. Therefore, impedance (Z) becomes

$$Z(\omega) = (v(t))/(I(t)) = (V_m \sin(\omega t))/(I_m \sin(\omega t+\vartheta)) = |Z|\exp(-i\theta)$$

When this is repeated over a large frequency range, it is represented as impedance spectra. From Euler's concept

$$Z(\omega) = |Z|\cos\theta+i|Z|\sin\theta$$

$$Z^* = Z'-iZ''$$

Where Z' and Z'' are the real and imaginary parts of the complex impedance measurements respectively. Impedance plot informs about different interfaces available in the cell. Depending on the electronically conducting nature of the sample (resistor, capacitor, inductor etc.) its impedance behavior can be modeled into different ways by variable combinations of R and C. For simple resistor, $Z'=R_{dc}$ and $Z''=0$ i.e. plot between Z' and Z'' will be a point on the real axis.

Ionic glassy samples are stated as a lossy capacitor and can be modeled as a parallel combination of the lossless capacitor (C) and resistor (R). The impedance of such solid system can be expressed as

$$Z^* = (R/i\omega C)/((R+ 1/i\omega C))$$

$$Z'-Z'' = R/(1+(\omega CR)^2)-i (\omega CR^2)/(1+(\omega CR)^2)$$

In above equation first term corresponds to the real part and the second term to the imaginary part of the impedance. Solving this equation and eliminating ω function,

$$(Z'-R/2)^2 + Z'' = (R/2)^2$$

Plot between |Z'| and |Z''| is a perfect semicircle with its center on the real axis. The diameter of the semicircle corresponds to the resistance of the sample. Many solid electrolytes exhibit depression in a semicircle at a higher frequency and an inclined line in a lower frequency. Phenomenon corresponding to an inclined line in lower frequency region represents interfacial polarization at electrode-electrolyte interface, whereas, depressed semicircle represents to parallel combination of constant phase element (CPE) [36] and resistance (R). An imperfect capacitor is modeled as CPE, space between the samples deviated it from ideal capacitive nature. The impedance of a CPE can be

$$CPE = 1/Q_0(i\omega)^n$$

Here, $Q_0 = 1/|z|$ at $\omega = 1$rad/s and $n \in [0, 1]$. Q and n are the fit parameters. For $n \rightarrow 1$, $Q_o \rightarrow C$ and $Z_{CPE} \rightarrow Z_C$. Generally, n is $(0 < n < 1)$ a frequency independent constant and n=0 or 1 determines the ideal resistor or an ideal capacitor nature respectively.

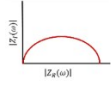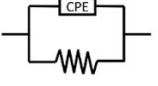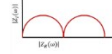Complex conductivity can be represented as
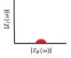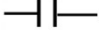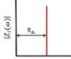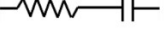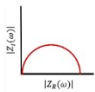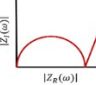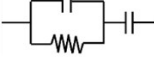
$$\sigma' = (l/|Z|A) = \cos\theta \text{ and } \sigma'' = (l/|Z|A) = \sin\theta$$

Here, l and A corresponds to length/thickness and cross-sectional area of the sample pellet. Phase angle (ϑ) can be represented as $\vartheta = \tan^{(-1)} (Z_I/Z_R)$. In polycrystalline samples, Cole-Cole plots are shown with two consecutive semicircles followed by an inclined line representing a parallel combination of resistance and constant phase element.

The conductivity of solid electrolytes can be described in terms of its frequency dependence. For this frequency region has been divided into three domains:

1. Low-frequency dispersion - Signifies polarization effect at the electrode and the electrolyte interface. Conductivity decreases in this region as more and more charges are accumulated with frequency reduction.

2. Intermediate frequency plateau - Conductivity is frequency independent in this region and it is equal to dc-conductivity.

3. High frequency extended dispersion - Conductivity increases with increase in frequency.

Table 2.3 - Impedance plots and their equivalent electrical circuits.

Plot	Z* (Plot and it's Nature)	Electrical Circuit
	R_d (Resistor)	
	$1/i\omega C$ (Capacitor)	
	$R + 1/i\omega C$ (Lossless capacitor (R and C in series))	
	$\left(Z_R - \dfrac{R}{2}\right)^2 + Z_1^2 = \left(\dfrac{R}{2}\right)^2 = Z_a$ (Parallel R and C)	
	$Z^2 + 1/(i\omega C)^2$ (Parallel R and C with C in series)	
	$1/R + 1/A(2\pi i f)^{-n}$ (Parallel R and CPE (lossy capacitor))	CPE
	$Z_a + Z_a$ (2 (parallel combination of R and C) in series)	

2.5.3 DC Polarization and Ionic Mobility.

DC Polarization [37] method was used to evaluate the contribution of electronic and ionic conductivity in total electrical conductivity. This is further used to calculate the electronic/ionic transport number of ions in the system.

Sample pellet (cylindrical in shape) is sandwiched in between blocking silver electrodes and the current is measured on different applied voltages (0.5V used here) as a function of time as shown in Fig. 2.14. For an ideal ionic sample, initially transient current drop rapidly and subsequently saturates to a constant value. Ionic transport number can be calculated from the following relation

$$t_i = \left[1 - \left(\frac{I_s}{I_o}\right)\right]$$

Where I_s is the saturated current and I_o is current at time t = 0.

Ionic mobility in a system can be measured using a transient current (TIC) technique as described elsewhere [38]. In this technique, the sample is polarized with a potential of 0.5V for 1 hour and then the polarity is reversed. The time taken by current to achieve its maximum value is obtained and that is defined as the time of flight (TOF = τ). Using the following formula, ionic mobility is measured as

$$\mu = D^2/V\tau.$$

For different thicknesses of the sample, the time of flight (τ) was measured and from the slope of $D^2/V\tau$ curve ionic mobility was obtained.
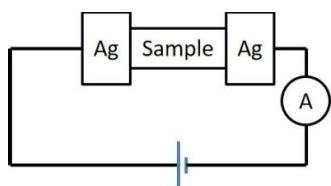

Fig. 2.13 Schematic diagram for DC polarization setup, power supply and ammeter interfaced with PC.
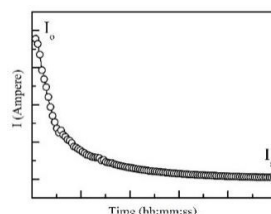
Fig. 2.14 Plot of transient current vs time for ionic sample on applying a dc voltage.

To understand the electrical transport process of Li^+ ions into the planned composites, Li^+ ion transport number has been determined. For the present study, ion transport number has been determined through two different methods viz; (i) Galvanic cell method and (ii) AC/DC method.

2.5.3.1 Galvanic Cell Method

It is also known as an electrochemical concentration cell method. This helps in determining the open circuit voltage (OCV) of the composites which informs about the role of Li^+ ions in charge transfer process. The procedure consists of two reference electrodes with a definite chemical potential of active species. Thermodynamically electromotive force (EMF) of the concentration cell is $\Delta G = -nE_NF$, where n is number of electrons transferred in the electrochemical cell reaction, F is Faraday's constant (96500 C mol^{-1}) and E_N is Nernst potential.

For ionic conductors, the measured open circuit (OC) voltage equals the calculated E_N, if the electrolyte is a pure conductor of corresponding mobile ion then transport number is

$$t_+ = \frac{OCV}{E_N} \qquad \text{or} \qquad t_+ = \frac{V_{obs}}{V_{cal}}$$

where, $V_{cal} = -\Delta G/nF$. OCP is the voltage difference and is measured directly across the cell. E_N is calculated from the thermodynamic Gibb's free energy of the reaction involved [39].

2.5.3.2 AC/DC Method

This is one of the most general procedures to calculate the ion transport number, particularly used for systems where cation's and anion's separate contributions require an assessment (e.g. polymers where anions exhibit significant transport). This procedure involves the analysis of ac impedance of a cell Li/Composite/Li. This is followed by applying small constant (dc current) potential difference between the electrodes. On application of a potential, current initially falls with time until a steady state current is obtained. Establishment of a concentration gradient across the cell is primarily responsible for the fall in current, and also may be due to (i) reduction of net moving ions, (ii) generation of an electromotive force (emf) which acts in opposite direction to the applied field and thus reduces the migration current of cations and anions, and (iii) increased motion of ions in the direction of the field to compensate the reduction in ion migration. Behavior of such cells was defined as $t^+ = I^s/I^o$, where I^s and I^o are steady state and initial cell current, respectively [40].

For small polarization and neglecting ion-ion electrostatic interactions, the initial and steady state current are given as

$$I^O = \frac{\Delta V}{(R_1^O + R_2)} = \frac{\Delta V}{(R_1^O + k/\sigma)} \tag{1}$$

And
$$I^S = \frac{\Delta V}{(R_1^S + kT_+\sigma)} \tag{2}$$

Where, ΔV is the potential across the cell, k is the cell constant, t^+ is the transport number, σ is the dc conductivity of the electrolyte, R_1^o and R_1^s are the initial and steady state resistance of the passivating layers and I^o and I^s are the initial and steady state current. From equation (1),

$$\sigma = I^o k / (\Delta V - I^o R_1^o) \qquad (3)$$

From equation (2) and (3) transport number can be calculated as

$$t_+ = \frac{I^s(\Delta V - I^o R_1^o)}{I^o(\Delta V - I^s R_1^s)} \qquad (4)$$

2.5.3.3 Cyclic Voltammetry [39]

It is an electrochemical technique which measures current as a response to applied voltage. Information regarding the thermodynamics and kinetics of any chemical reaction can be determined. The whole experimental setup consists of three different electrodes. (i) working electrode, (ii) counter/auxiliary electrode and (iii) reference electrode (fig. 2.15).
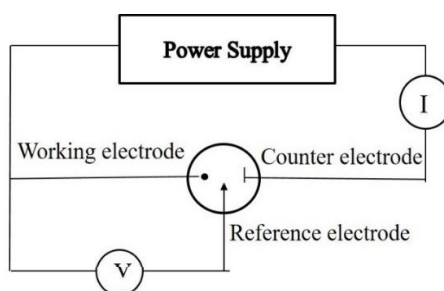

Fig. 2.15 Experimental setup for Cyclic Voltammetry

In the experiment, the voltage of a working electrode *vs* a reference electrode is measured in a voltaic cell. The voltage is increased linearly in a linear sweep *vs* time for the working electrode cycled against a counter electrode. For solid electrolytes, C and R are joined and the sample is sandwiched in between W and C+R electrodes. Thus, the property of solid electrolyte is studied in a two-probe geometry using CH instrument (Series 1200) potentiostat/galvanostat. In present work, cyclic voltammetry is used for measuring the electrochemical potential window for some electrolytes and understanding the capacitive properties of some composites (in detail in chapter 5).

2.6 Other Compositional Studies

2.6.1 Gravimetric Estimation

This is a classical technique for elemental analysis which measures the amount of element/compound after some chemical treatment and separation in a particular form [41]. The procedure involves analyzing the element of interest by weight in the form of a precipitate which is insoluble and can be easily separated by filtration (as such or after ignition). From the weight of the obtained product the % of the element in the sample can be readily calculated. This method has many advantages and few disadvantages, but above all, it is a very precise, cheaper and absolute method for quantitative analysis of compounds/composites. The analysis is time-consuming and there are some error possibilities, for example, (i) due to small particle size (0.1 nm or 10 nm) and (ii) due to super saturation.

In this work elements analyzed is lead (Pb) which was precipitated as lead chromate ($PbCrO_4$). The sample is initially digested with HNO_3. For this method potassium chromate (4%) was used as a precipitating reagent, washing was done using a buffer mixture of (4% sodium acetate). $Pb^{2+} + CrO_4^{2-} \rightarrow PbCrO_4$.

Pb content in glass is estimated as follows: Let us assume X g of sample gives Y g of $PbCrO_4$. Then the amount Pb in X g of sample is given as: (207.21/323.2)*Y, where relative atomic mass of Pb is 207.21 and relative molar mass of $PbCrO_4$ is 323.2. The % of Pb obtained thus can be compared with % expected based on the initial mixture used for glass formation.

2.6.2 Density measurements and Molar Volume estimations.

Normally the amorphous (glassy) substances will have low density and higher molar volume compared crystalline substances of the same composition.

In density measurements crushed powder of the composite/gel is used. The densities of gels were measured with xylene as the density standard (density = 0.861 gm/cm$^{3)}$ and using specific gravity bottles (pycnometer) purchased from BOROSIL of volume 5 ml and 10 ml. Measurements were repeated at least two times for each composite and the density values are accurate to ±0.05 g/cm^3.

To calculate the density of the sample four readings were taken with the help of density bottle, viz; (i) Empty density bottle (W1), (ii) Density bottle filled with xylene (W2), (iii) Density bottle with the sample (W3) and (iv) Density bottle with sample and xylene (W4). Then the density of the sample is given as $\rho_s =$[(W3 $-$ W1) x ρ_x] / [(W2 + W3) $-$ (W1 + W4)]. Where ρ_x is the density of xylene.

Molar volume was calculated using relation: $V_m = M/\rho$, where V_m is molar volume, ρ is the density of the sample, and M is the relative molar mass of the sample.

2.7 Software used.

In this work the following sets of software were used for the purposes mentioned.

- Origin pro 8.5 for plotting spectral and other data,
- Chem-Draw Ultra 12.0 for drawing chemical structures,
- eisanalyzer software - fitting of impedance plots.
- In house developed FORTRAN codes for EPR spectral simulations and X-ray Pair Distribution Functions.

References:

1. 1. Horowitz F., Dawnay E.J.C., Fardad M.A., Green M., Yeatman E.M., "Towards Better Control of Sol-Gel Film Processing for Device Applications", *Journal of Nonlinear Optical Physics & Materials* **6** (1997) 1-18.

2. K. Kamiya, "Sol–Gel-Prepared Glass and Ceramic Fibers" in L. Klein et al. (eds.), "Handbook of Sol-Gel Science and Technology", Springer International Publishing Switzerland (2016).

3. H. Schmidt., "New Type of Non-Crystalline Solids between Inorganic and Organic Materials" Journal of Non-Crystalline Solids **73** (1985) 681-691.

4. Ulrich Schubert, Nicola Hiising, Anne Lorenz, "Hybrid Inorganic-Organic Materials by Sol-Gel Processing of Organofunctional Metal Alkoxides", *Chemistry of Materials.* **7** (1995) 2010-2027.

5. Serena Esposito, "Traditional' Sol-Gel Chemistry as a Powerful Tool for the Preparation of Supported Metal and Metal Oxide Catalysts", *Materials* **12** (2019) 668-692.

6. Ebelmen J. J., *Ann.* **57**(1846) 331.

7. Brinker C. J., Scherer G. W., "Sol-gel science: The Physics and Chemistry of Sol-Gel Processing", Academic Press (2013).

8. R. Brenier, J. Mugnier, E. Mirica, "XPS study of amorphous zirconium oxide films prepared by sol–gel", *Applied Surface Science* **143** (1999) 85–91.

9. Saloua Rezguif, Bruce C. Gates, Sandra L. Burkett, Mark E. Davis, "Chemistry of Sol-Gel Synthesis of Aluminum Oxides with in Situ Water Formation: Control of the Morphology and Texture", *Chemistry of Materials* **6** (1994) 2390-2397.

10. H. Schmidt, "Chemistry of Material Preparation by the Sol-Gel Process" *Journal of Non-Crystalline Solids* **100** (1988) 51-64.

11. Larry L Hench, Jon K West, "The Sol-Gel Process." *Chemical Review* **90** (1990) 33-72.

12. R. K. Iler, "The colloid chemistry of silica and silicates", Cornell University Press, Ithaca, New York (1955).

13. R. Aelion, Loebel A., Eirich F., "Hydrolysis of ethyl silicate", *Journal of the American Chemical Society* **72** (1950) 5705-5712.

14. J. Pouxviel, Boilot J., Beloeil J., Lallemand J., "NMR study of the sol-gel polymerization", *Journal of Non-Crystalline Solids* **89** (1987) 345-360.

15. P. Muralidharan, Satyanarayana N., Venkateswarlu M., "Structural, ac Conductivity and Electric Modulus Studies of Lithium Based Quaternary Silicate Glasses Synthesised by the Sol-Gel Route." *Physics and Chemistry of Glasses* **46** (2005) 293-301.

16. A. Vioux, "Nonhydrolytic Sol-Gel Routes to Oxides", *Chemistry of Materials* **9** (1997) 2292-2299.

17. B. D. Cullity, "Elements of X-ray Diffraction", Addison-Wesley Publishing Company, Inc., Reading, Massachusetts (1956).

18. H. P. Klug, Alexander L. E., "X-ray diffraction procedures: For polycrystalline and amorphous materials". 2nd Edition, Wiley-VCH (1974).

19. P. Raghunathan, S.C. Sivasubramanian, "Structural Characterization of Some Novel Ternary $PbO-PbCl_2-CuCl_2$ Glasses by X-Ray Pair Distribution Functions, Thermal Analysis and Electron Paramagnetic Resonance." *Journal of Non-Crystalline Solids* **136** (1991) 14-26.

20. P. B. Ayscough, "Electron Spin Resonance in Chemistry", Methuen, London (1967).

21. P. H. Rieger, " Electron Spin Resonance – Analysis and Interpretation", The Royal Society of Chemistry, Cambridge UK (2007).

22. P. Raghunathan, S. C. Sivasubramanian, "Magnetic resonance lineshapes in powdered and amorphous systems", *Proceedings of the Indian Academy of Sciences (Chemical Science)* **96** (1986) 565-580.

23. P. Raghunathan, S. C. Sivasubramanian, "X-ray Diffraction, Electron Paramagnetic Resonance, and Electron Spin Echo Modulation Studies of the PbO-$PbCl_2$,-$CuCl_2$, Ternary Glass System", *Journal of Physical Chemistry,* **95** (1991) 6346-6351.

24. G. E. Peterson, C. R. Kurkjian, A. Carnevlae, "Random Structure Models and Spin-Resonance In Glass", *Physics and Chemistry of Glasses* **15** (1974) 52-58.

25. A. Portis, "Electronic structure of F centers: Saturation of the electron spin resonance", *Physical Review* **91** (1953) 1071-1078.

26. A. Stoneham, "Shapes of inhomogeneously broadened resonance lines in solids", *Reviews of Modern Physics* **41** (1969) 82-108.

27. Barbara Stuart, " Infrared Spectroscopy: Fundamentals and Applications", John Wiley and Sons Ltd., West Sussex, England (2004).

28. Nicolas Brodusch, Hendrix Demers, Raynald Gauvin, "Field Emission Scanning Electron Microscopy: New Perspectives for Materials Characterization", Springer, Singapore (2018).

29. John F. Watts, John Wolstenholme, "An Introduction to Surface Analysis by XPS and AES", John Wiley & Sons, Ltd, West Sussex, England (2003).

30. Paul van der Heide, "X-ray photoelectron spectroscopy: An introduction to principles and practices", John Wiley & Sons, New Jersey (2012).

31. G. W. H. Höhne, Hemminger W., Flammersheim H. J., "Differential Scanning Calorimetry", Springer-Veriag, Berlin (2003).

32. Peter J. Haines, "Thermal Methods of Analysis: Principles, Applications and Problems", Springer Science + Business Media, Dordrecht (1995).

33. E. Barsoukov, J. R. Macdonald,., "Impedance spectroscopy: Theory, experiment, and applications", 2nd Edition, Wiley (2005).

34. J. H. Sluyters, "On the impedance of galvanic cells-I. Theory", *Recueil des Travaux Chimiques des Pays-Bas* **79** (1960) 1092-1100.

35. J. H. Sluyters, J. J. C. Oomen, "On the impedance of galvanic cells-II. Experimental verification", *Recueil des Travaux Chimiques des Pays-Bas* **79** (1960) 1101-1110.

36. S. M. Haile, West D. L., Campbell J., "The role of microstructure and processing on the proton conducting properties of gadolinium-doped barium cerate", *Journal of Materials Research* **13** (1998) 1576-1595.

37. R. C. Agrawal, Gupta R. K., "Superionic solid: Composite electrolyte phase - An overview", *Journal of Materials Science* **34** (1999) 1131-1162.

38. M. Rathore, Dalvi A., "Effect of conditional glass former variation on electrical transport in $Li_2O–P_2O_5$ glassy and glass-ceramic ionic system", *Solid State Ionics* **263** (2014) 119-124.

39. A. J. Bard and L. R. Faulkner, "Electrochemical Methods: Fundamentals and Applications", 2nd Edition, John Wiley & Sons Inc., New York (2001).

40. J. Evans, C. A. Vincent, P. G. Bruce, "Electrochemical measurement of transference numbers in polymer electrolytes", *Polymer* **28** (1987) 2324 – 2328.

41. A.I. Vogel, "A Textbook of Quantitative Inorganic Analysis", 4th Ed., Longman Green, London (1978).